

Attention Enhanced 3D-U-Net++ Ocean Temperature and Salinity Reconstruction in the Northwestern Pacific based on Transfer Learning

Hao Wang^{1,2,3}, Linlin Zhang^{2,4}, Shuguo Yang³, Xiaomei Yan^{2,4}, Zhen Li^{2,4}

5 ¹ College of Electromechanical and Engineering, Qingdao University of Science and Technology, Qingdao, 266061, China

² Key Laboratory of Ocean Observation and Forecasting and Laboratory of Ocean Circulation and Waves, Institute of Oceanology, Chinese Academy of Sciences, Qingdao, 266071, China

³ College of Mathematics and Physics, Qingdao University of Science and Technology, Qingdao, 266061, China

⁴ University of Chinese Academy of Sciences, Beijing, 101408, China

10 *Correspondence to:* Linlin Zhang (zhanglinlin@qdio.ac.cn)

Abstract. Real-time and accurate three-dimensional ocean temperature-salinity (T-S) field are of great significance for a deeper understanding of ocean dynamics and prediction skill improvement of numerical models. However, current ocean observations, especially those below the sea surface, still suffer from significant limitations in temporal and spatial resolution. Several neural network methods using multi-source satellite data for underwater temperature and salinity reconstruction have been proposed, achieving real-time temperature and salinity reconstruction, but their biases relative to in-situ observations are still significant. This study focuses on the northwestern Pacific region (0–40°N, 120–160°E) and proposes an attention-enhanced three dimensional U-Net++ model, which reconstructs daily T–S fields (26 layers, 1/4° resolution, 5–2000 m depth) using real-time available sea surface temperature (SST) and sea surface height (SSH) data. The model introduces cross-scale feature aggregation and selective information gating, allowing it to emphasize temporally coherent surface features most relevant to subsurface variability, while suppressing noise propagation and over-smoothing. By integrating 26 consecutive days of SST and SSH as inputs, the model effectively alleviates the underdetermined problem of mapping limited surface observations to full-depth structures. In addition, a two-stage transfer learning strategy is employed: the model is first pretrained using monthly SST/SSH data and the gridded Argo data to learn observation-dominated low-frequency spatiotemporal patterns, and then fine-tuned using daily SST/SSH data and the high-resolution reanalysis to capture the meso-scale dynamic processes. Evaluation results demonstrate that the reconstructed T-S fields exhibit better agreement with in-situ T-S profiles from World Ocean Database than previous studies, both during the validation period and in long-term statistical analyses, indicating the reliability and accuracy of the proposed approach for subsurface ocean field reconstruction. The reconstructed T-S field is available at <https://doi.org/10.57760/sciencedb.31950> (Wang et al., 2025).

30 1 Introduction

The three-dimensional (3D) temperature and salinity (T-S) fields of the ocean are the most fundamental parameters characterizing the marine environment. Investigations of the three-dimensional T-S fields have provided crucial insights into oceanic dynamical processes, climate variability, and the evolution of marine ecosystems (Curry et al., 2003; Gill, 2016). However, the available in-situ observational data remain extremely sparse in both spatial coverage and temporal resolution (Stewart, 2008), rendering them insufficient for resolving the fine-scale structures and evolution of meso-scale phenomena (Pauthenet et al., 2022). Consequently, the hydrological gridded data reconstructed from these observations also exhibit limited temporal and spatial resolution.

Satellite remote sensing provides global observations of ocean surface parameters (Klemas and Yan, 2014), including sea surface height (SSH), sea surface temperature (SST), and sea surface salinity (SSS), with the advantages of high temporal and spatial resolution. However, these measurements are restricted to the ocean surface and cannot directly capture the subsurface density structure (Talley et al., 2011; Klemas and Yan, 2014). Fortunately, a strong physical coupling exists between the surface and subsurface layers of the ocean. The temperature, salinity, and current structures beneath the surface are closely linked to surface conditions through the exchange of heat and momentum within the seawater (Munk, 1950; Huang, 2010). This intrinsic coupling makes it feasible to reconstruct subsurface T-S fields from surface observations (Fu and Davidson, 1996; Ali et al., 2004; Wu et al., 2012).

Early studies on T-S reconstruction primarily relied on statistical regression (Guinehut et al., 2012), interpolation, or physics-based models (Gilson et al., 1998; Willis et al., 2003). These methods have enabled the estimation of the ocean's vertical structure to some extent. However, the applicability and accuracy are constrained by the discrepancy between the linear assumptions and the inherently nonlinear nature of the real ocean. For instance, reconstruction approaches based on the Surface Quasi-Geostrophic (SQG) approximation assume that surface density variations are entirely governed by temperature (Isern-Fontanet et al., 2006; Lacasce and Mahadevan, 2006), neglecting the influence of salinity and other nonlinear factors. As a result, such methods struggle to accurately represent the complex vertical structures observed in the actual ocean. In recent years, obtaining subsurface temperature and salinity fields through data assimilation has become another important approach (Chen et al., 2025; Martin et al., 2025). On one hand, satellites can provide large-scale and high-frequency sea surface information, and assimilating these observations helps improve the simulation of subsurface temperature and salinity structures (Fu, 2016). On the other hand, existing temperature and salinity observation profiles can be directly used in data assimilation models to further refine the simulated subsurface structures (Bellucci et al., 2007). Although satellite data assimilation has become a major means of obtaining subsurface temperature and salinity fields and

has shown good performance in surface and near-surface layers, there remain significant challenges in accurately reproducing the vertical structures of mesoscale eddies (Pilo et al., 2018; Gwyther et al., 2023).

65 With the rapid development of deep learning, neural networks have demonstrated great potential in the reconstruction of oceanic temperature and salinity fields due to their powerful nonlinear fitting capabilities (Wu et al., 2012; Xie et al., 2025). In recent years, various neural network-based temperature and salinity reconstruction methods have emerged, which can be broadly categorized into four types: point-to-point, surface-to-point, surface-to-surface, and surface-to-volume approaches. Point-to-point methods use sea surface data together with geographical coordinates (latitude and longitude) as network inputs to estimate subsurface temperature and salinity at corresponding locations (Chen et al., 2022). These
70 methods typically adopt architectures such as Long Short-Term Memory (LSTM) or Back Propagation (BP) neural networks (Su et al., 2021; Su et al., 2022; Smith et al., 2023). The surface-to-point approach uses surface data from a small surrounding region to reconstruct the subsurface temperature and salinity at the central point of that region, typically using convolutional neural networks (CNNs) (Zhao et al., 2025). For example, Meng et al. (2021) developed a 2D-CNN and reconstructed subsurface temperature and salinity anomalies (STA, SSA) at the regional center using $20^\circ \times 20^\circ$ patches of
75 Sea level anomaly, sea surface temperature anomaly, sea surface salinity anomaly and wind stress anomaly (SLA, SSTA, SSSA, and WSA). The surface-to-surface approach reconstructs subsurface temperature and salinity fields layer by layer with surface data in a given region (Su et al., 2019), and usually adopts a U-Net architecture (Song et al., 2024; Zhang et al., 2024). The surface-to-volume approach reconstructs three-dimensional subsurface fields (i.e., full-depth temperature and salinity) for a region directly from surface data, typically using neural networks with 3D encoder-decoder architectures
80 (Mao et al., 2023). Notably, this approach involves a mapping from limited input information (surface data) to a much larger output space (multi-depth fields), a process analogous to super-resolution tasks, which remains a considerable challenge.

At present, data-driven neural network reconstruction methods are evolving toward multi-source data fusion. Early studies
85 primarily relied on SST and SSH, whereas later research incorporated additional inputs such as sea surface wind (SSW) and SSS. More recently, studies have even included surface wind stress curl derived from surface wind fields. The inclusion of multiple data sources provides more effective input features, thereby improving reconstruction accuracy (Wu et al., 2012; Cheng et al., 2021; Wang et al., 2021; Yu et al., 2025; Zhao et al., 2025).

90 However, among current satellite datasets, only SST and SSH are available in real-time, whereas SSW and SSS data exhibit latencies of approximately 1–3 days and 3–7 days, respectively. Consequently, to realize real-time reconstruction of subsurface temperature and salinity using neural networks, the input variables are restricted to the real-time accessible SST

and SSH. To achieve real-time large-depth reconstruction of subsurface temperature and salinity, this study proposes a method that relies solely on real-time available SST and SSH data. The method is based on an attention-enhanced 3D U-Net++ architecture, which effectively captures multi-scale spatial features and deep coupling relationships. A transfer learning strategy introduced by (Pan and Yang, 2010) is also employed: the network is first pre-trained using monthly SST, SSH, and Argo gridded T-S products to learn real observational information and large-scale temporal patterns; then, it is fine-tuned using daily SST, SSH, and a well-recognized Global Ocean Reanalyses and Simulations Stream 2 version 4 data (GLORYS2V4) to capture daily dynamic processes and characteristics. To address the challenge of reconstructing full-depth fields from limited input data, a long time-series input strategy is introduced, where a sequence of past surface observations is used as input. Results show that this strategy could significantly improve the accuracy of full-depth T-S reconstruction. The study area, spanning 0°N–40°N and 120°E–160°E, is a dynamically active region of global significance, strongly influenced by major circulation systems such as the Kuroshio and North Equatorial Current. The model successfully reconstructs temperature and salinity from 5 m to 2000 m. Results demonstrate that the model achieves higher reconstruction accuracy than several widely used datasets across both validation and long-term sequences, and shows closer agreement with World Ocean Database (WOD) in-situ T-S profiles. It indicates that the proposed neural network is capable of generating subsurface fields that are consistent with reanalysis data and show superior alignment with observational profiles under surface constraints. Thereby it provides a feasible and efficient framework for the real-time 3D reconstruction of ocean temperature and salinity fields.

110

The remainder of this paper is organized as follows: Section 2 presents the data and methods used in this study. The data section introduces the neural network training data employed in this work and the comparative data used for quality analysis. The methods section provides a detailed description of the attention-enhanced 3D U-Net++ model, the transfer learning training strategy, and the approach of using long-term time series of sea surface data as network inputs. Section 3 presents the results and analysis, including comparative analyses of different transfer learning training strategies, the impact of using long-term time series of sea surface data as network inputs on reconstruction results, and the reliability analysis of the model-reconstructed temperature and salinity data. Section 4 concludes the paper.

115

2 Data and Methods

2.1 Data

2.1.1 Training Data

120

The SST data used in this study were obtained from the Optimum Interpolation Sea Surface Temperature (OISST) dataset provided by the National Oceanic and Atmospheric Administration (NOAA) (Huang et al., 2021). This dataset has a global

spatial resolution of $0.25^\circ \times 0.25^\circ$ and a daily temporal resolution. It integrates satellite observations from multiple platforms with various in situ measurements. The dataset is publicly available at: <https://www.ncei.noaa.gov/data/sea-surface-temperature-optimum-interpolation/v2.1/access/avhrr/>.

The SSH data were provided by the Archiving, Validation, and Interpretation of Satellite Oceanographic Data (AVISO) program. This dataset is derived from the integration of multiple satellite altimeter missions, which have undergone rigorous calibration, validation, and data assimilation processes. It provides a spatial resolution of $1/8^\circ$ and a daily temporal resolution. The dataset can be accessed at: <https://doi.org/10.48670/moi-00148>.

During the pretraining stage of the neural network, the gridded Argo product developed by the International Pacific Research Center (IPRC) was used as the target data. This dataset was generated through a variational interpolation algorithm applied to Argo float observations, with a spatial resolution of $1^\circ \times 1^\circ$ and a monthly temporal resolution. It is available at: https://apdrc.soest.hawaii.edu/projects/Argo/data/gridded/On_standard_levels/index-1.html.

For the fine-tuning stage, daily temperature and salinity fields from the GLORYS2V4 reanalysis dataset were employed as the ground truth. The GLORYS2V4 dataset provides global ocean reanalysis fields on a 0.25° grid by assimilating observational data into an ocean circulation model. It enables comprehensive analysis of ocean dynamics and contributes to improved weather and climate predictions. The dataset is available at: <https://doi.org/10.48670/moi-00024>.

It is worth noting that due to differences in the temporal and spatial resolutions of the label data used in the two stages of transfer learning, the datasets were unified for this study. The specific data processing methods are detailed in Table 1.

Table 1. Data processing and normalization methods.

Training Stage	Training Set	Validation Set	Data	Data Processing Method	Normalization Method
Pre-training	2005-2019	2020	AVISO SSH	Downsampling to 0.25° Monthly averaging	Standardization followed by
			OISST	Monthly averaging	Min-Max normalization
			RPRC Argo	Linear interpolation to 0.25°	Min-Max normalization only
Fine-tuning	1993-2022	2023	AVISO SSH	Downsampling to 0.25°	Standardization followed by
			OISST	None	Min-Max normalization
			GLORYS2V4	None	Min-Max normalization

In the pre-training phase, the input data were averaged monthly to match the temporal resolution of the IPRC Argo temperature and salinity data. Additionally, to be consistent with the OISST data and match the output dimensions of the neural network, both the 1/8° resolution AVISO SSH data and the IPRC Argo data were linearly interpolated to 0.25°. In the fine-tuning phase, since both the training data and label data are daily records, no temporal averaging was performed; however, the 1/8° AVISO SSH data were down-sampled to 0.25°.

Furthermore, the data normalization strategies differed between the two stages. As the pre-training data predominantly contain monthly signals, the label data were simply normalized to the range of [0, 1]. In contrast, for the fine-tuning phase—where the objective was for the network to learn smaller time-scale signals (i.e., abrupt changes) based on the pre-trained model—the label data were first standardized using the mean and standard deviation, and then normalized to [0, 1]. To ensure consistency, the input data for both stages were processed using the same two-step approach: standardization followed by [0, 1] normalization.

2.1.2 Validation data

To objectively assess the reliability of the reconstructed products, this study employed quality-controlled T-S profiles from the WOD for error analysis (Mishonov et al., 2024). The profiles provided by the XBT have been used after correction (Cheng et al., 2014). The WOD dataset is publicly available at: <https://www.ncei.noaa.gov/products/world-ocean-database>.

The High-Resolution Northwest Pacific Temperature Salinity Current Dataset was also utilized. This dataset integrates historical hydrographic observations from CTD and Argo floats with recent satellite altimeter data. It is derived using the Height Geostrophic Empirical Mode (HGEM) method (Zhang and Sun, 2012), which reconstructs three-dimensional ocean

temperature, salinity, and velocity fields based on large-scale continuous satellite altimetry observations. The dataset has a spatial resolution of $0.25^\circ \times 0.25^\circ$ and a temporal resolution of one week. It is available at: <https://msdc.qdio.ac.cn/data/metadata-special-detail?id=1456480706929647617&otherId=1456480709660139521>.

170

The China Global Ocean Fusion Dataset 1.0 (CGOF1.0) was also adopted for comparative analysis. This dataset extensively integrates more than 40 publicly available global ocean environmental datasets together with China's officially released ocean data. It employs a data–physics hybrid intelligent big data methodology and a sparse observation data migration and reconstruction technique. The dataset has a spatial resolution of $1/12^\circ$ and a temporal resolution of one month.

175 It can be accessed at <https://www.cmoc-china.cn/pages/CGOF.html>.

The global reanalysis product from the Hybrid Coordinate Ocean Model (HYCOM) was also utilized in this study. This system employs the Navy Coupled Ocean Data Assimilation (NCODA) scheme to assimilate available satellite altimeter observations, sea surface temperature, and in-situ vertical temperature and salinity profiles. HYCOM utilizes a unique hybrid coordinate system that transitions between isopycnal coordinates in the open ocean, z-level coordinates in the mixed layer, and sigma coordinates in shallow coastal regions. The dataset typically features a spatial resolution of $1/12^\circ$ and a temporal resolution of one day. It is accessible at: <https://www.hycom.org/dataserver>.

The Ocean Reanalysis System 5 (ORAS5) produced by the European Centre for Medium-Range Weather Forecasts (ECMWF) was introduced for comparative analysis. Based on the NEMO ocean model coupled with the LIM2 sea-ice model, it utilizes the NEMOVAR variational data assimilation methodology to integrate extensive in-situ and satellite observations. ORAS5 provides a consistent historical reconstruction of the ocean state with a spatial resolution of 0.25° and a temporal resolution of one day. The dataset can be accessed at: <https://www.ecmwf.int/en/forecasts/dataset/ocean-reanalysis-system-5>.

190 **2.2 Methods**

2.2.1 3D-UNet++

The U-Net++ architecture used in this study is a deep learning network originally designed for image segmentation tasks. It was proposed as an enhanced version of U-Net (Zhou et al., 2018). Its structure is illustrated in Fig.1 (a). U-Net++ employs an encoder–decoder architecture with deep supervision and a series of dense skip connections between the encoder and decoder. Convolutional layers are introduced along the skip pathways to reduce the semantic gap between feature maps of the encoder and decoder. The dense skip connections play a pivotal role in bridging the semantic gap between the encoder and decoder feature maps. Unlike the simple long skip connections in the standard U-Net, these nested, dense

200 pathways pass feature maps through a series of convolutional blocks before fusing them with the decoder. This process gradually aggregates features at varying semantic levels, ensuring that the decoder receives more semantically rich and consistent information. Consequently, this mechanism allows the network to capture complex multi-scale features more effectively—acting essentially as an ensemble of U-Nets—which significantly improves gradient flow during training and enhances segmentation accuracy for objects of diverse sizes.

205 The deep supervision mechanism in U-Net++ can operate in two modes: precise and fast. In the precise mode, outputs from all sub-branches are averaged to generate the final segmentation map, while in the fast mode, only one segmentation branch is used, which also allows for model pruning. By performing multi-level feature fusion, U-Net++ effectively utilizes hierarchical feature information, transmitting low-level details to high-level semantic representations, thereby improving both the accuracy and boundary sharpness of the reconstruction results.

210 The 3D-U-Net++ network employed in this study is derived from the conventional U-Net++ architecture by replacing all 2D operations—such as convolution, pooling, and up-sampling—with their 3D counterparts. Notably, 3D convolution is capable of simultaneously processing data across four dimensions: depth, channel, height, and width (Tran et al., 2015). This capability renders the network highly suitable for physical oceanographic datasets, which typically encompass spatial extent, depth, and temporal information.

215 Building on this foundation, to further enhance the model’s capability in handling the complex task of temperature–salinity reconstruction and to improve its ability to capture the importance of different local and channel-wise features, a Convolutional Block Attention Module (CBAM) was integrated into the network. The architecture of CBAM is shown in Fig.2 (a). CBAM aims to strengthen the representational power of convolutional neural networks by focusing on the most relevant features across both spatial and channel dimensions (Woo et al., 2018). By combining channel attention and spatial attention, CBAM provides a more comprehensive and effective feature extraction mechanism, thereby improving the representational capability of the 3D U-Net++. CBAM consists of two main components: the Channel Attention Module (CAM) and the Spatial Attention Module (SAM), whose structures are illustrated in Fig.2 (b) and (c), respectively.

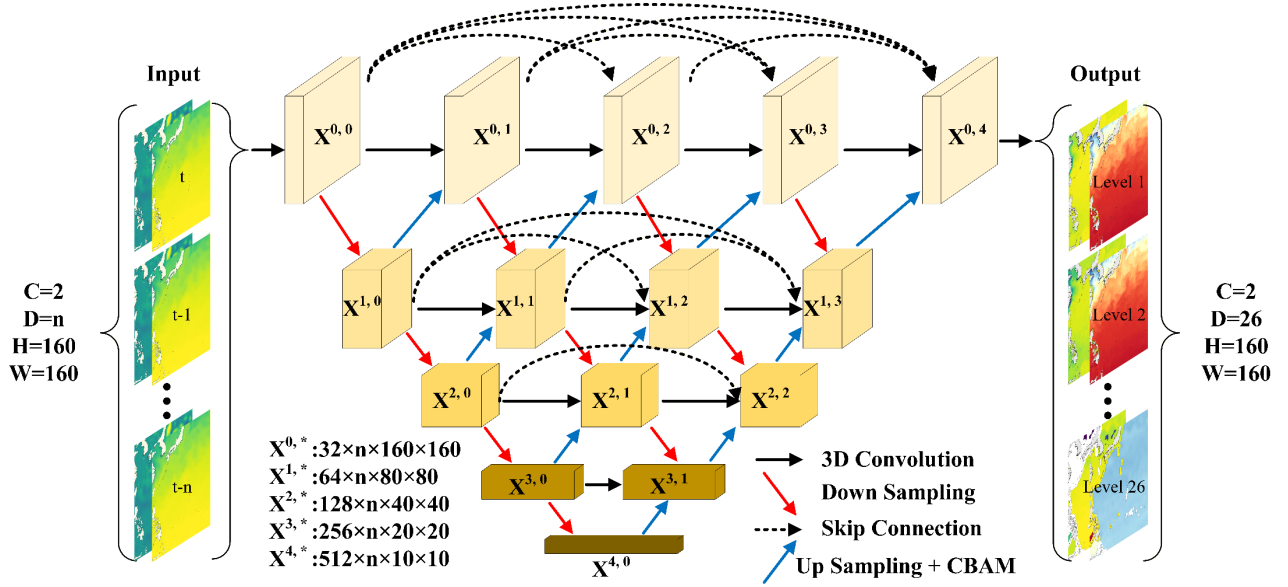


Figure 1. Schematic diagram of the 3D-U-Net++ neural network structure, where $X^{i,j}$ represents the feature map at level i and stage j .

As illustrated in Fig. 1, the neural network is designed to directly accept a 4D tensor with a shape of $(C \times D \times H \times W)$ as input. In this study, C is set to 2, representing the two input channels: SSH and SST. D is set to 26, denoting the continuous time series of sea surface data from the past 26 days (details regarding D are provided in Section 2.2.3). H and W are both set to 160, corresponding to the spatial dimensions of the study area. The output dimensions of the network are (2, 26, 160, 160). Specifically, the first dimension 2 represents the two target variables: seawater temperature and salinity; 26 corresponds to 26 depth levels spanning from 0 to 2000 m; and 160 represents the spatial dimensions of the study area. Within the network architecture, down-sampling is performed using 3D max pooling, while up-sampling is achieved via 3D transposed convolution.

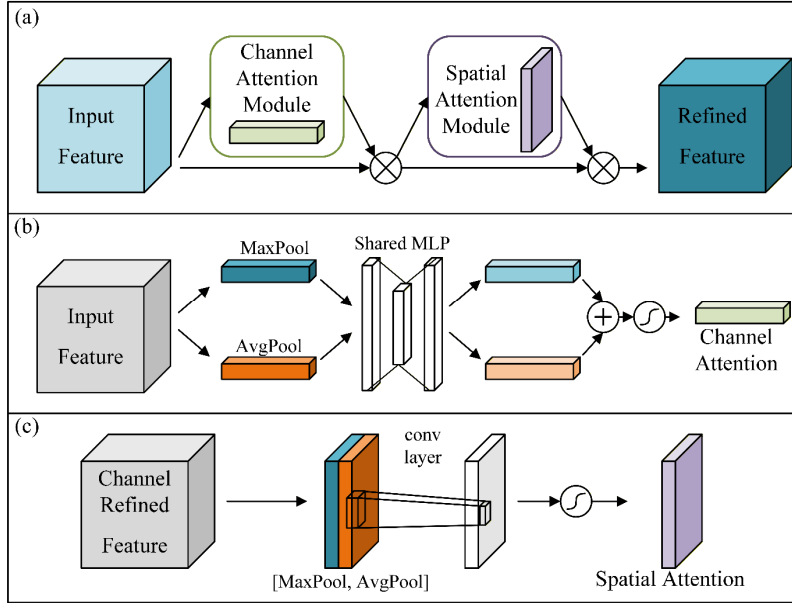


Figure 2. (a) Network structure diagram of CBAM. (b) CAM branch in CBAM. (c) SAM branch in CBAM.

The CAM operates by learning which channels in the feature maps are more important, thereby enhancing the most informative channels while suppressing irrelevant ones. Specifically, the module first aggregates spatial information via global average and max pooling. It then applies a shared multi-layer perceptron (MLP) to generate channel-wise attention. The computational process of this module can be expressed as follows:

$$M_c(F) = \sigma \left(MLP(AvgPool(F)) + MLP(MaxPool(F)) \right) \quad (1)$$

where $M_c(F)$ is output of the CAM, $\sigma()$ represents the sigmoid activation function, $MLP()$ represents the multilayer perceptron, $AvgPool()$ and $MaxPool()$ represent mean pooling and max pooling, respectively. F is the input feature.

240

The SAM focuses on the spatial locations of features, learning where the most important regions lie within the spatial domain. It first applies global average pooling and max pooling along the channel dimension, concatenates the resulting feature maps, and then performs a convolution operation to generate a spatial attention map that highlights key spatial areas. The computational process of SAM can be expressed as follows:

$$M_s(F) = \sigma(f^{7 \times 7 \times 7}([AvgPool(F); MaxPool(F)])) \quad (2)$$

where $M_s(F)$ is output of the CAM, $\sigma()$ represents the sigmoid activation function, $f^{7 \times 7 \times 7}()$ denotes a 3D convolution operation with a kernel size of $7 \times 7 \times 7$, $AvgPool()$ and $MaxPool()$ represent 3D mean pooling and 3D max pooling, respectively. F is the input feature.

250 Together, CAM and SAM enable the CBAM to selectively emphasize informative features, reduce irrelevant information, and enhance the discriminative capability of the model. Consequently, CBAM improves model performance across various tasks such as classification, detection, and segmentation.

2.2.2 Transfer Learning

To enhance the generalization capability of the model and enable it to extract features across different data modalities, 255 thereby learning the common characteristics shared by observational and reanalysis datasets, this study employed a transfer learning strategy during neural network training.

Transfer learning is a paradigm in machine learning whose fundamental concept is to transfer knowledge acquired from one task (the source domain) to improve learning performance on another related task (the target domain) (Pan and Yang, 260 2010). The transfer learning framework adopted in this study is illustrated in Fig. 3.

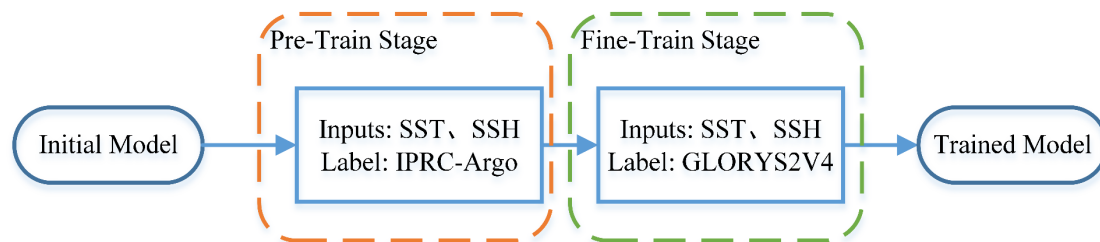


Figure 3. Overview of Transfer Learning Strategies

In this study, model training was conducted in two distinct stages. During the pretraining stage, monthly mean SST and SSH fields were used as input data, while the IPRC-Argo gridded temperature and salinity products served as the target labels. This stage enabled the model to learn from real observational information and capture large-scale monthly signals. In the retraining (fine-tuning) stage, daily SST and SSH data were used as inputs, and the GLORYS reanalysis dataset was 265 adopted as the target. This allowed the model to learn the physical patterns and data assimilation mechanisms embedded within the reanalysis data.

2.2.3 Long-Term Sea Surface Time-Series as Input for Model Training

This study aims to achieve high-accuracy reconstruction of subsurface temperature and salinity across 26 depth layers (5–2000 m) using a neural network. The input data include SST and SSH, while the outputs are multi-level subsurface 270 temperature and salinity profiles.

The main challenge of this task lies in the fact that traditional methods typically rely only on single-time (t) sea surface observations to infer the corresponding three-dimensional temperature–salinity structures, as shown in Fig. 4a. Because the input feature dimension is relatively low while the output space is high-dimensional, the model must recover complex vertical structures from limited surface information. This imposes strict demands on the network’s ability to capture and generalize spatial–temporal relationships. In essence, this problem is analogous to super-resolution reconstruction, characterized by information insufficiency and non-uniqueness.

To address this limitation, we introduce an improved strategy that incorporates temporal sequence information. Specifically, the network input is extended from a single-time snapshot to a continuous days sequence of surface observations, spanning from $t-a$ to t , as show in Fig. 4b. This design leverages the temporal evolution of oceanic processes, enabling the network to learn the dynamic relationships governing subsurface thermal and haline structures.

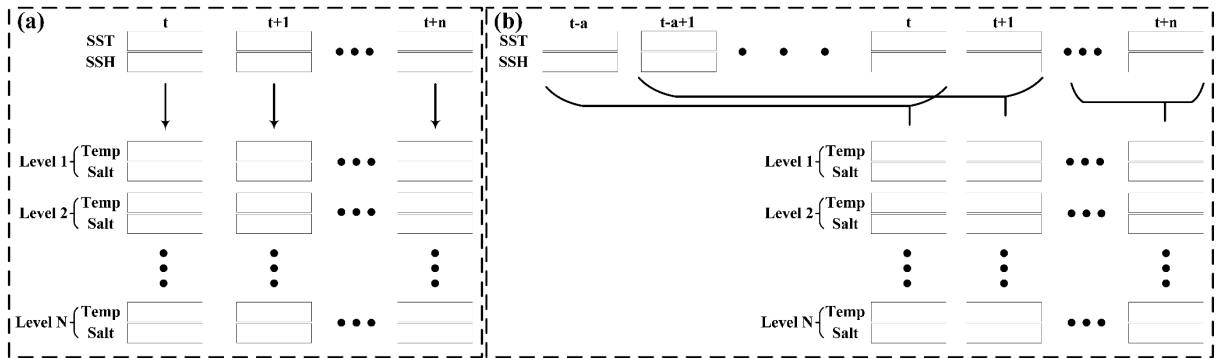


Figure 4. Two different data input approaches. (a) Temperature and salinity reconstruction using single-day sea surface data, where n denotes the total time length and t represents the time step. (b) Temperature and salinity reconstruction using consecutive multi-day sea surface data, where n denotes the total time length, t represents the time step and a represents the time window length.

3 Result

Model training and inference were conducted on a supercomputing cluster equipped with an Intel® Xeon® Gold 5218R CPU and an NVIDIA A100-PCIE-40GB GPU. The average inference time required to generate daily 3D T-S fields for the entire region is approximately 5 seconds. In contrast to traditional reanalysis products (e.g., GLORYS and EN4) which typically suffer from latencies ranging from weeks to months due to the assimilation of sparse in-situ data (see Table 2), our method relies exclusively on real-time satellite observations, enabling real-time reconstruction using data from the current day.

Table 2. Comparison of update cycles and approximate time lag (latency) between the proposed method and mainstream products.

Dataset / Product	Type	Approximate Update Cycle / Latency	Dependence on In-situ Data
Proposed Method	Deep Learning Reconstruction	Daily / No lag	No (Only relies on NRT Satellite SST & SSH)
GLORYS12V1 (CMEMS)	Reanalysis	Monthly / ~2-3 years lag (Delayed Mode)	Yes (High dependence)
PSY4V3R1 (CMEMS Analysis)	Operational Analysis	Weekly / ~7 days lag (Best estimate)	Yes
EN4 (Met Office)	Objective Analysis	Monthly / ~1-2 months lag	Yes
RG-Argo (Scripps)	Gridded Argo Product	Monthly / ~1-2 months lag	Yes
SODA3	Reanalysis	Monthly / Several months lag	Yes

3.1 Transfer Learning

295 To identify the optimal transfer learning approach, multiple transfer learning strategies were tested by conducting comparative experiments in this study. These included freezing only the encoder, freezing only the decoder, and freezing network weights at different percentage positions from the input to the output layers. In the comparative experiments, inputs spanning multiple months and multiple days were employed for the pre-training and fine-tuning stages, respectively. The pre-training phase utilizes data from the preceding a consecutive months, whereas the fine-tuning phase employs data from the preceding a consecutive days (refer to Section 3.2 for the specific value of a).

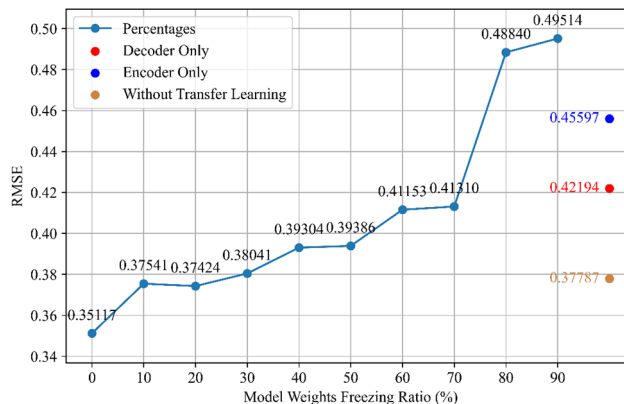


Figure 5. Average RMSE between model outputs and WOD T-S profiles data during 2023 under different transfer learning strategies

As illustrated in Fig. 5, the comparative results demonstrate that the reconstruction performance of the neural network varies significantly under different transfer learning strategies. When the model was trained solely using the GLORYS2V4 reanalysis data without applying transfer learning, the baseline RMSE reached 0.3779, which is consistent with the RMSE between the 2023 GLORYS T-S data and the WOD T-S profiles (see Section 3.3.2). This indicates that when the network is trained only on GLORYS2V4 data, its overall accuracy approaches that of GLORYS itself.

When transfer learning was applied by freezing the encoder, the RMSE increased to 0.4560, whereas freezing the decoder produced an improved RMSE of 0.4219. Further analysis of gradually freezing network layers from the input to the output revealed a non-monotonic pattern. The lowest RMSE of 0.3512 was obtained when no layers were frozen, indicating full adaptability during fine-tuning. When 10 %–30 % of the network was frozen, the model achieved relatively good performance with RMSE values close to the baseline. However, when more than half of the network parameters were frozen, the RMSE increased sharply.

The experimental results demonstrate that the optimal transfer learning strategy is global fine-tuning (0% frozen weights), rather than acting as a rigid feature extractor (which would favor partial freezing). This indicates that the fundamental mechanism of transfer learning in this study is providing a physically constrained parameter initialization rather than directly reusable features. Oceanographically, the transfer process mimics a “background-to-perturbation” learning paradigm. During the pre-training phase with monthly, coarse-resolution IPRC Argo data, the network learns the large-scale climatological background, encompassing basic stratification, seasonal cycles, and global vertical covariance structures. By establishing this robust physical framework, the pre-trained weights place the model in a physically plausible region within the high-dimensional optimization landscape. During the fine-tuning phase with daily, high-resolution GLORYS data, global fine-tuning allows the network to bypass the struggle of learning fundamental ocean physics from scratch. Instead, it fully allocates its learning capacity to resolving high-frequency, synoptic-scale dynamics—such as how mesoscale eddies and fronts perturb the pre-established climatological background.

In summary, since the neural network is trained exclusively on GLORYS2V4 data, the error between the reconstructed data and the WOD observational profiles can only asymptotically approach the error between the label data and the WOD profiles. Initializing the network weights using the IPRC Argo dataset allows the model to capture authentic observational information while establishing a background of the ocean environment at a monthly scale. Building upon this foundation, the fine-tuning phase enables the network to learn the complex dynamic mapping rules and smaller time-scale signals

inherent in the GLORYS2V4 data. Validation against WOD profile data demonstrates that this transfer learning strategy maintains high physical consistency with GLORYS2V4 while achieving closer agreement with the WOD observations.

335 In this study, a transfer learning strategy without weight freezing was adopted, in which the model was fine-tuned on GLORYS2V4 data after pre-training.

3.2 Input Time Series Data

To determine the optimal length of the input time series for the network, an ablation study was conducted. Considering computational costs, time series lengths of 1, 4, 8, 10, 20, 26, 30, and 40 days were selected. The experimental results are 340 illustrated in Fig. 6, which demonstrate a clear negative correlation between the input sequence length and the reconstruction error. When the time step increases from 1 to 20, the RMSE for both variables decreases significantly—Temperature RMSE drops from 0.63563°C to 0.61222°C, and Salinity RMSE from 0.09874 PSU to 0.09475 PSU. This indicates that the incorporation of historical surface data helps to mitigate the ambiguity associated with super-resolution tasks. Furthermore, continuous time-series of sea surface data provide robust physical constraints for the reconstruction of 345 underwater 3D T-S fields, thereby enhancing the accuracy of the reconstructed data.

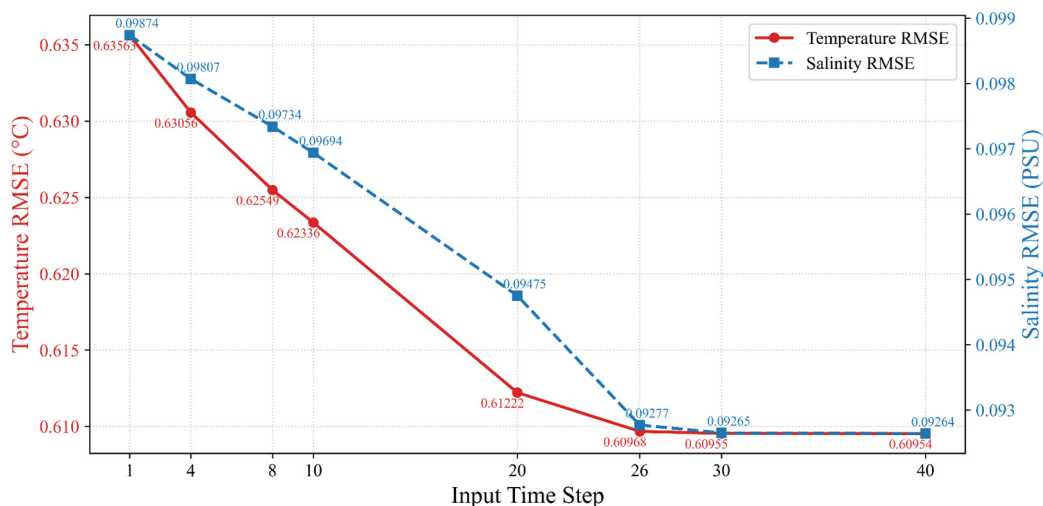


Figure 6. RMSE between the reconstructed data and WOD profiles under different input time series lengths in 2023.

Notably, the performance gain begins to saturate beyond an input length of 26 days. Between time steps 30 and 40, the RMSE curves for both temperature and salinity plateau (stabilizing around 0.6095°C and 0.0926 PSU, respectively). To balance computational cost and accuracy, the time series length of the input data was set to 26 in this study.

3.3.1 Comparison of the Model Reconstructions with GLORYS2V4

Figure 7 and Figure 8 respectively present the vertical profiles of RMSE and correlation coefficients for temperature and salinity, with curves for different months illustrating seasonal variations and vertical characteristics.

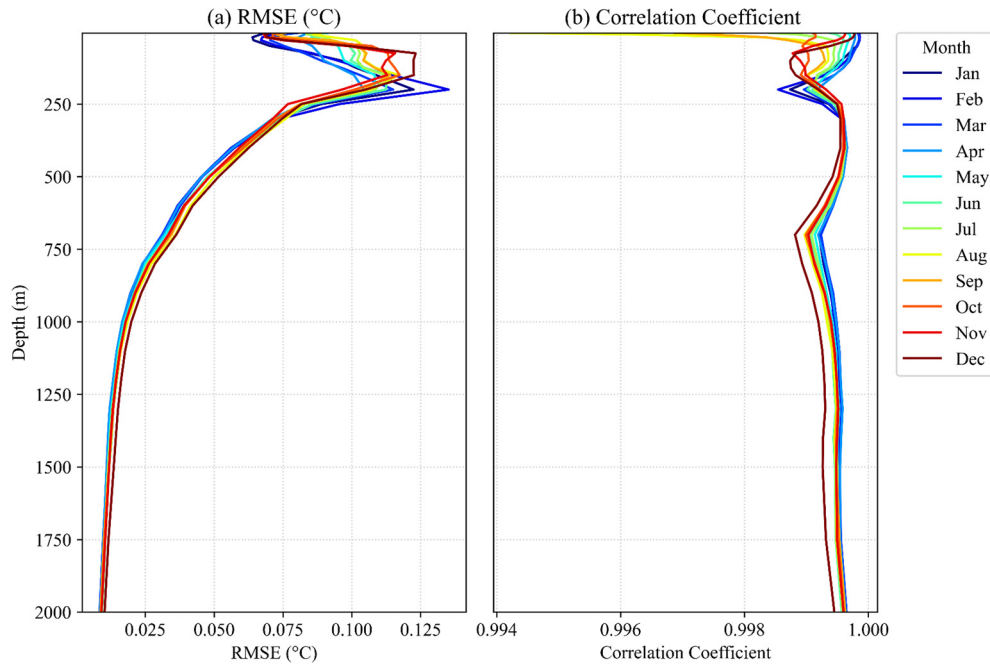


Figure 7. (a) RMSE and (b) correlation coefficient between the model-reconstructed temperature fields and the GLORYS2V4 temperature data in 2023.

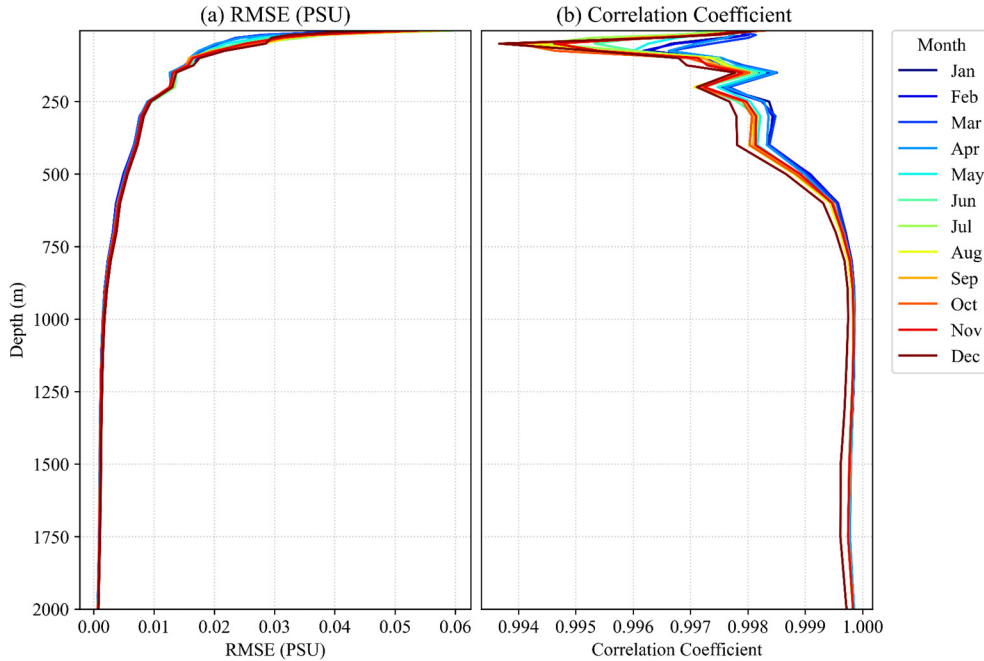


Figure 8. (a) RMSE and (b) correlation coefficient between the model-reconstructed salinity fields and the GLORYS2V4 salinity data in 2023.

355 From the RMSE distribution of temperature reconstruction (Fig. 7a), the overall RMSE ranges between 0.025°C and 0.125°C. Above 250 m, the temperature RMSE increases with depth, while below 250 m it gradually decreases, stabilizing at depths greater than 1000 m with relatively low values (approximately within 0.015°C). This trend indicates that the neural network model effectively captures the stable structure of deep-sea temperatures, though certain deviations persist in the subsurface layers influenced by atmospheric forcing and mixed-layer dynamics. The correlation coefficients (Fig. 360 7b) remain above 0.99 across all depths, demonstrating strong consistency and indicating that the model preserves the linear response relationship of temperature variations well.

The reconstructed salinity RMSE (Fig. 8a) generally decreases with depth, with surface RMSE values ranging from 0.02 to 0.06 PSU. In deeper layers (>1000 m), the RMSE markedly decreases, approaching 0 PSU, suggesting that the model accurately reproduces the salinity structure in deep ocean regions. The overall correlation coefficients remain above 0.99 (Fig. 8b), showing slight fluctuations in the upper layers but minimal variation among months, reflecting the model's strong capability to reproduce the spatiotemporal distribution patterns of salinity.

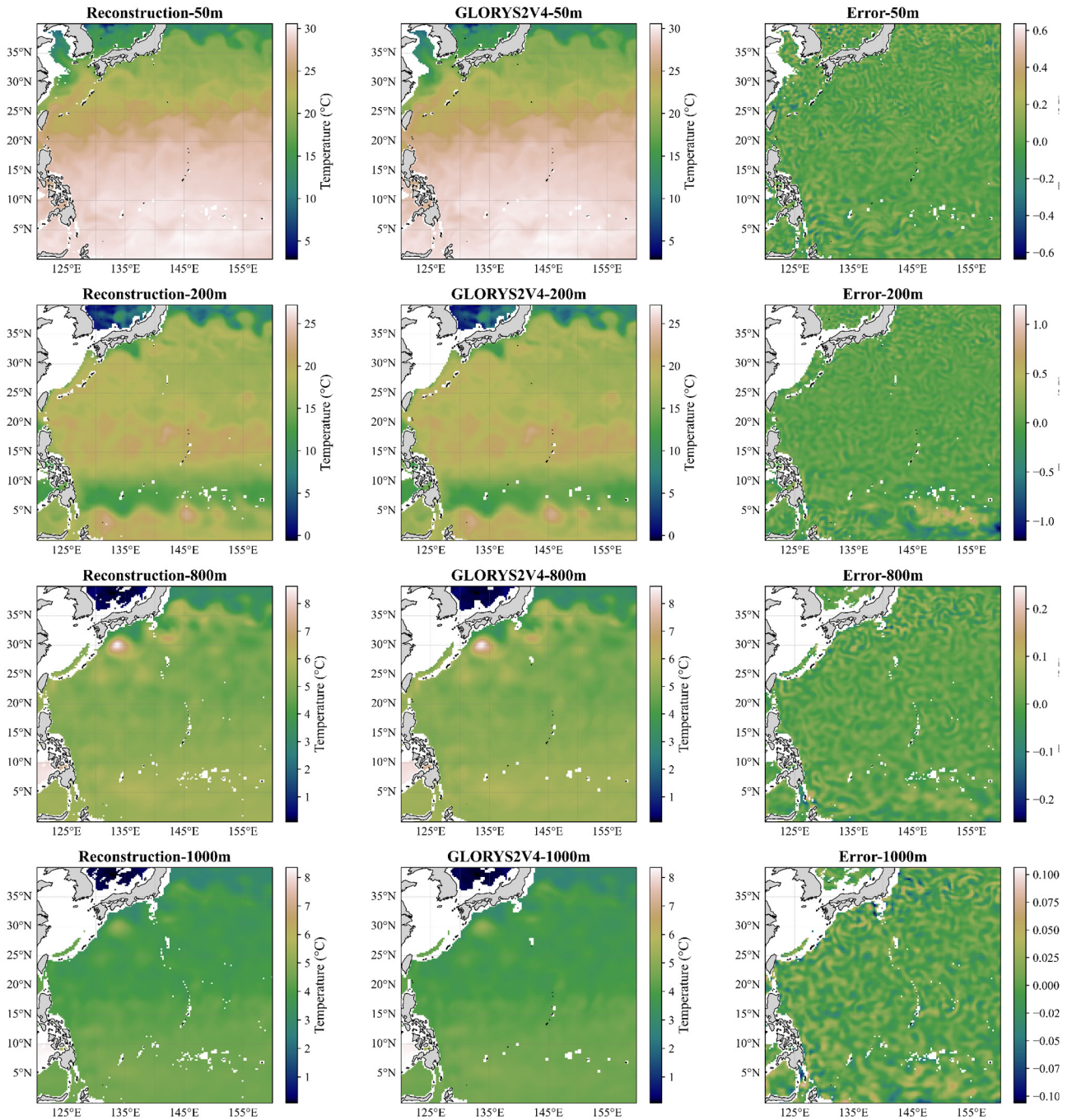


Figure 9: Reconstructed temperature (left) and GLORYS2V4 temperature (middle) and their differences (right) at depths of 50 m, 200 m, 800 m, and 1000 m on January 1, 2023.

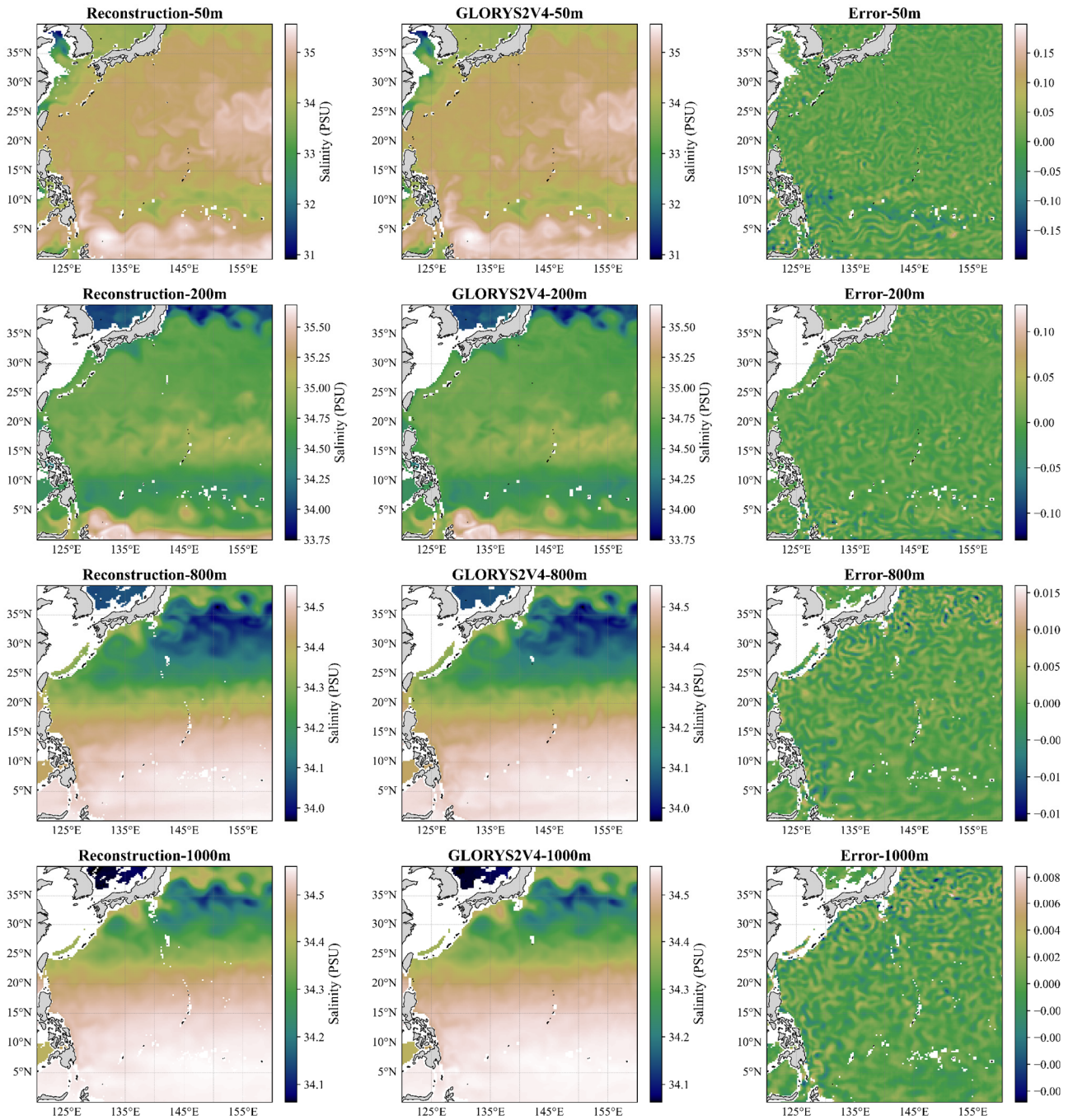


Figure 10: Reconstructed salinity (left) and GLORYS2V4 salinity (middle) and their differences (right) at depths of 50 m, 200 m, 800 m, and 1000 m on January 1, 2023.

As shown in Fig. 9 and Fig. 10, the reconstructed temperature and salinity fields exhibit spatial patterns that are highly consistent with those of the GLORYS2V4 data, successfully reproducing the latitudinal gradients and large-scale thermohaline structures. The error maps reveal that the magnitude of the discrepancies is limited and relatively uniform across the study region, with no areas of concentrated error and near-zero differences in most regions. At greater depths, such as 800 m and 1000 m, the errors further decrease and no systematic bias is observed, indicating the enhanced stability and reliability of the model in deep-ocean environments.

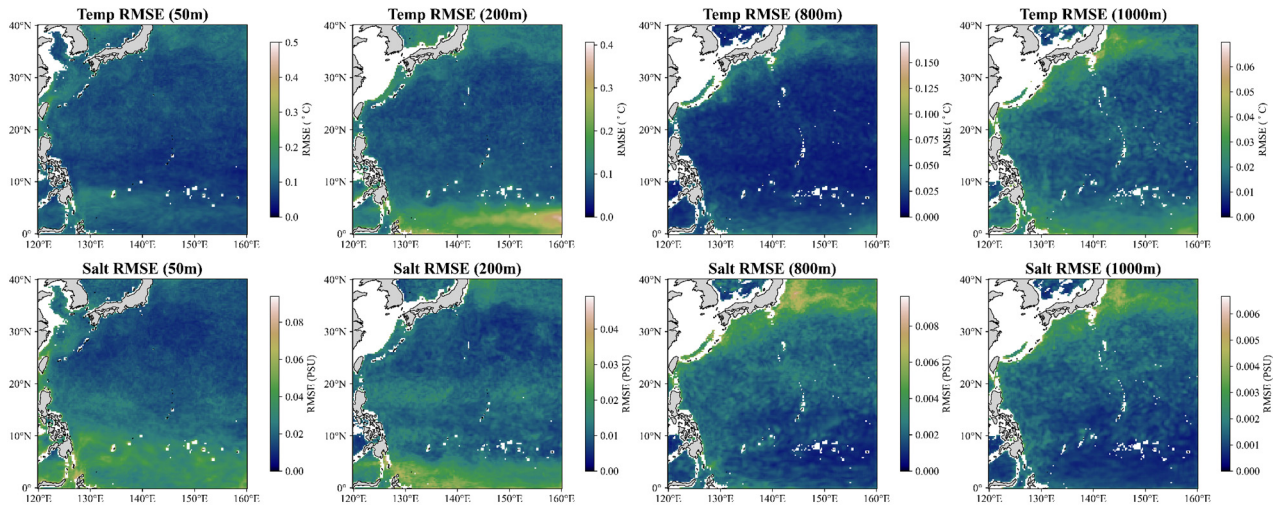


Figure 11. Spatial distribution of the RMSE between the reconstructed data and the GLORYS2V4 data at depths of 50 m, 200 m, 800 m, and 1000 m in 2023.

Figure 11 illustrates the spatial distribution of the RMSE at different depths throughout the validation period. It can be observed that at depths of 50 m and 200 m, the RMSE of the validation set is primarily concentrated in the North Equatorial Countercurrent (NECC) region. In contrast, at 800 m and 1000 m, the RMSE is mainly concentrated in the Kuroshio Extension region. Overall, however, the RMSE across all four depth levels remains within a relatively low range throughout the entire study area.

These findings confirm that the proposed neural network can effectively infer subsurface thermal structures using only surface observational data. The high spatial consistency and low reconstruction errors across all depths highlight the model's strong generalization capacity. The particularly robust performance in the intermediate and deep layers underscores its ability to capture stable, large-scale oceanic states.

385 3.3.2 Comparison of the Model Reconstructions with WOD T-S Profiles

To objectively evaluate the reliability of the reconstructed products, WOD T-S profiles data were introduced for error analysis. After quality control, a total of 7,833 T-S profiles were selected within the study region for the year 2023, as shown in Fig. 12a.

390 At the geographical coordinates corresponding to each T-S profile, reconstructed temperature and salinity data as well as GLORYS2V4 temperature and salinity data were extracted to compute the RMSE. The vertical RMSE distributions between the WOD T-S profiles and the reconstructed and GLORYS2V4 T-S data are shown in Figs. 12b-c.

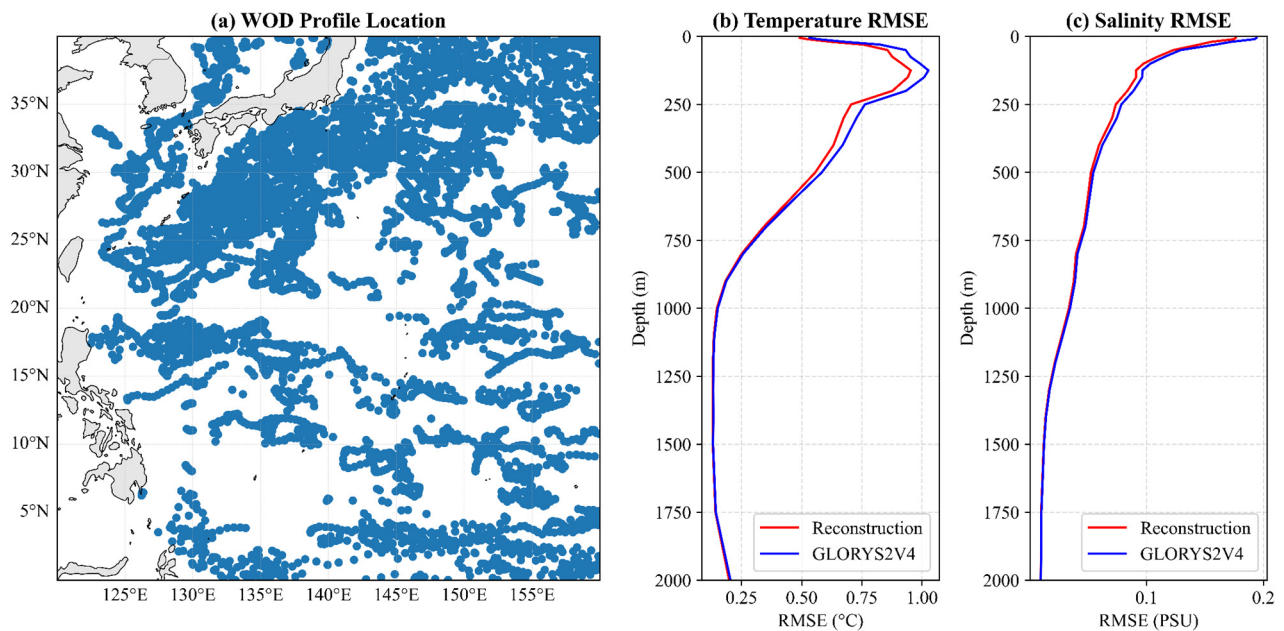


Figure 12: (a) Spatial distribution of WOD observational profiles in 2023; (b) variation of temperature RMSE with depth between the reconstructed temperature data and the WOD temperature profiles; (c) variation of salinity RMSE with depth between the reconstructed salinity data and the WOD salinity profiles.

In 2023, the T-S profiles distribution within the study region was relatively uniform (Fig. 12a). Overall, the reconstructed and the GLORYS2V4 T-S data exhibit similar vertical RMSE distributions (Figs. 12b and 12c). For temperature, both datasets show higher RMSE values in the subsurface layers (Fig. 12b), while for salinity, the RMSE values decrease gradually with depth (Fig. 12c). The reconstructed T-S data generally outperform the GLORYS results at all depths. The mean RMSE of the reconstructed temperature over the full depth range is 0.4907 °C, lower than that of GLORYS (0.5241 °C). Similarly, the mean RMSE of the reconstructed salinity (0.0699 PSU) is slightly lower than that of GLORYS

395

(0.0747 PSU). Clearly, the reconstructed T-S fields show closer agreement with the in situ observations, indicating better
400 reconstruction fidelity.

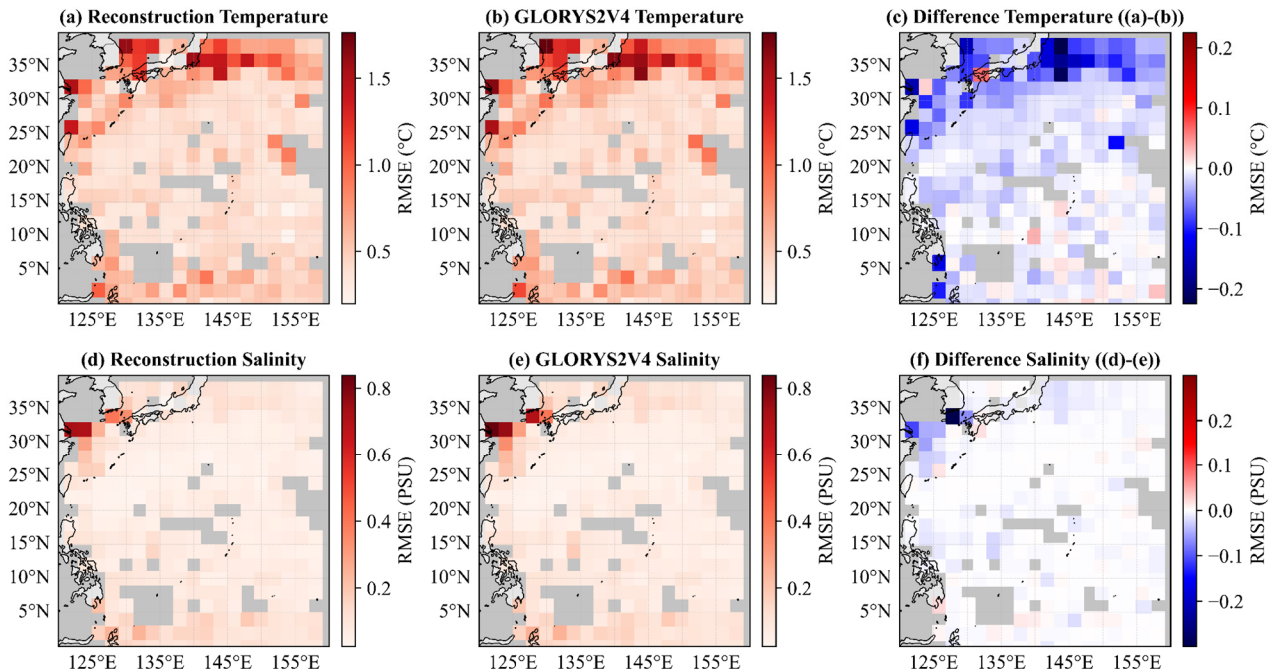


Figure 13. RMSE between reconstruction and WOD profiles (left), RMSE between GLORYS2V4 and WOD profiles (middle), and their difference (right). The first row shows the results for temperature data, and the second row shows the results for salinity data.

The spatial distribution of the RMSE between the reconstructed data and the WOD profiles is shown in Fig. 13. Spatially, both datasets exhibit larger errors along the western boundary currents and near-coastal regions, while the errors are relatively smaller in the interior of the basin (Figs. 13a-b, and d-e). The difference maps indicates that the reconstructed temperature and salinity, especially the temperature, generally performs better across the study region (Figs. 13c and f).
405 Overall, the reconstructed T-S fields derived from the neural network are more consistent with the WOD T-S profiles, demonstrating higher reliability.

Since the 3D-U-Net++ model learns the mapping from surface (SST, SSH) to subsurface layers based on the statistical relationships embedded in GLORYS2V4, the reconstructed outputs inevitably inherit the structural characteristics of this
410 specific reanalysis product. However, this does not imply that the model merely reproduces the reanalysis climatology. As shown in Figs. 12-13, The high consistency between the reconstruction and the independent WOD profiles demonstrates that the model successfully generalizes the learned relationships to actual oceanic conditions, rather than simply overfitting to the reanalysis statistics. This confirms that the method reconstructs independent oceanic variability driven by surface

inputs, while utilizing the reanalysis data to constrain the vertical thermohaline structure. Therefore, the reconstructed
415 product should be interpreted as a combination of real-time satellite-observed surface variability and the dynamical vertical
structure learned from GLORYS2V4.

3.4 Long-term Statistical Analysis

To further verify the robustness and reliability of the proposed reconstruction method in generating T-S data, a long-term
statistical analysis of the reconstructed results was conducted. Specifically, after the neural network training was completed,
420 SST and SSH data from 1993 to 2023 were used as inputs to reconstruct the corresponding T-S fields for the same period.
The reconstructed results were then compared with all available WOD T-S profile observations from 1993 to 2023 to
perform an error analysis. For the long-term comparison, six reference datasets—GLORYS2V4, HYCOM, ORAS5,
HGEM, IPRC Argo, and CGOF—were employed.

425 During the period from 1993 to 2023, a total of 353,154 WOD T-S profiles were collected within the study region. For
clarity of presentation, the RMSE values calculated from these samples were averaged on a monthly basis. The RMSE
results for temperature and salinity are presented in Fig. 14 and Fig. 15, respectively. Since the valid time span of the IPRC
Argo dataset is 2005–2020, the results were divided into three distinct periods to better demonstrate the effectiveness of
the transfer learning strategy: 1993–2004 (Figs. 14a and 15a), 2005–2019 (Figs. 14b and 15b), and 2020–2023 (Figs. 14c
430 15c). The variation of RMSE with depth was also calculated based on the WOD samples, and the results are shown in Fig.
15.

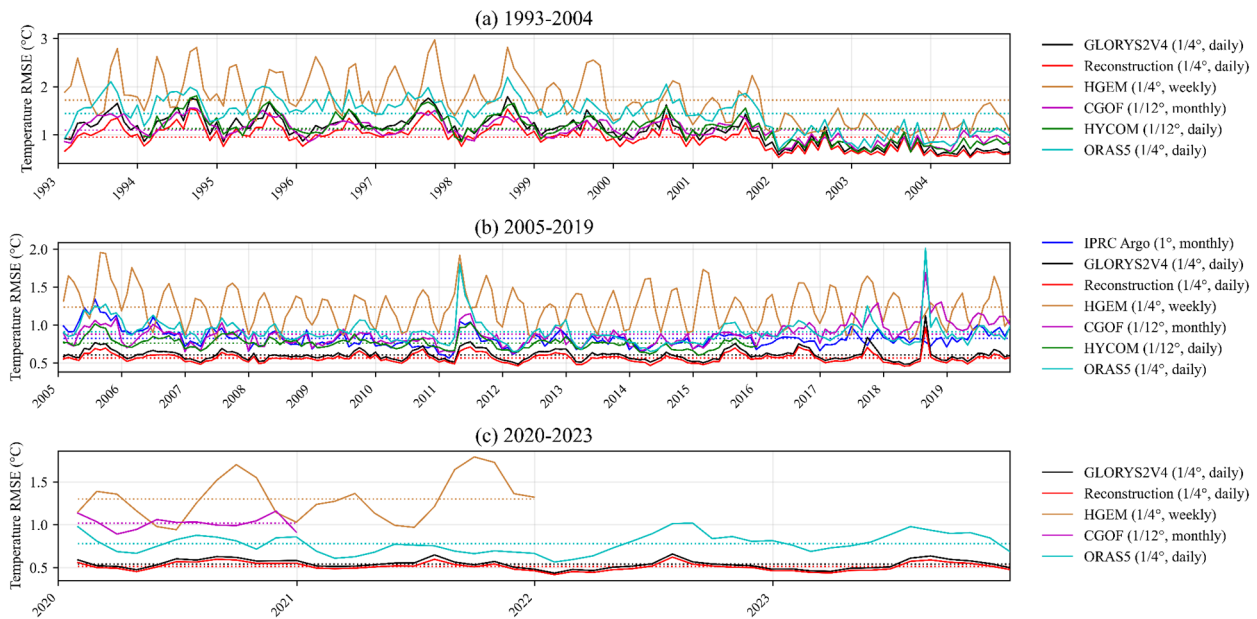


Figure 14. Monthly time series of RMSE of various temperature datasets compared with WOD temperature profiles in the upper 2000m: (a) 1993–2004, (b) 2005–2019, and (c) 2020–2023.

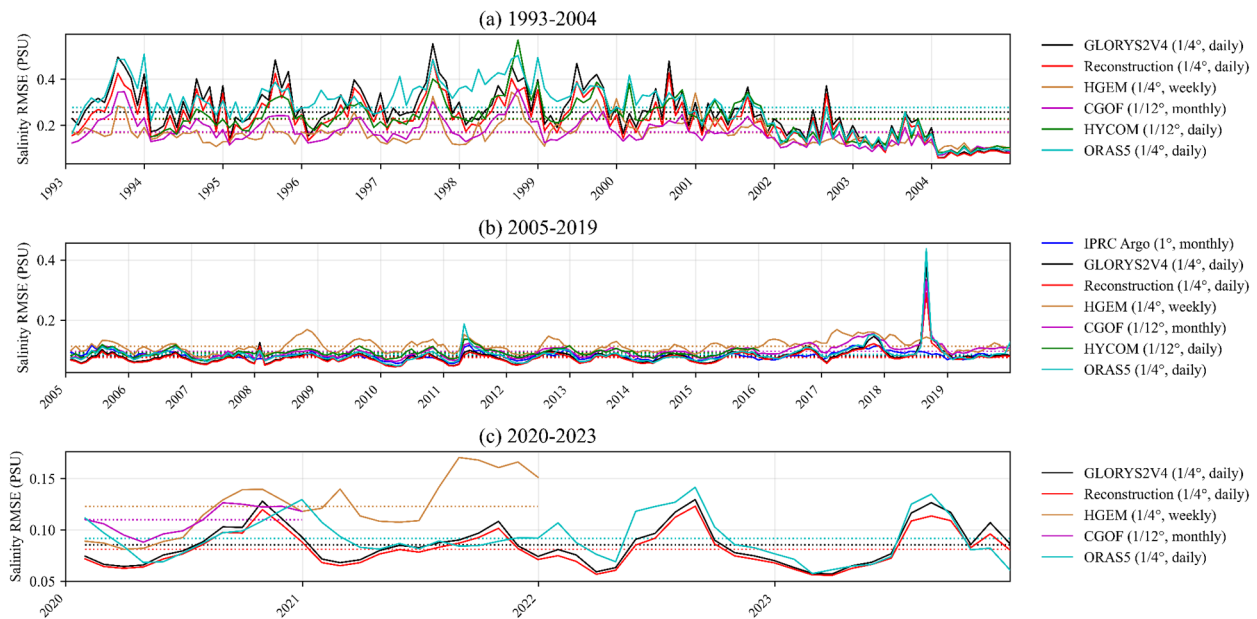


Figure 15. Monthly time series of RMSE of various salinity datasets compared with WOD temperature profiles in the upper 2000m: (a) 1993–2004, (b) 2005–2019, and (c) 2020–2023.

As shown in Fig. 14, throughout the entire study period (1993–2023), the reconstructed temperature field remains generally consistent with GLORYS2V4. Compared with all other reference datasets, the reconstructed temperature results are closer to the WOD observed temperature profiles (Average RMSE: 0.677267 °C), demonstrating higher accuracy and reliability.

Regarding the RMSE results for salinity, during 1993–2004, HGEM exhibits the smallest errors (0.1681PSU) among the compared datasets (Fig. 15a); however, in the subsequent periods, the reconstructed salinity data align more closely with the WOD salinity profiles, indicating better stability and adaptability of the proposed method in salinity reconstruction.

Throughout the entire period (1993–2023), the reconstructed salinity shows the closest agreement with the WOD observed salinity, with an RMSE of 0.1282 PSU.

It can also be observed that the RMSE values of all datasets are relatively high during 1993–2004. This is mainly because the number of WOD T-S profiles during this period was limited, and most observations were concentrated along the Japanese coast. This region lies within the highly dynamic Kuroshio Current zone, where the vertical thermohaline structure exhibits strong cross-front differences and prominent mesoscale to submesoscale variability, resulting in larger assimilation errors between model outputs and observations.

Notably, in the proposed transfer learning strategy, the pretraining data were derived from the 2005–2019 IPRC Argo T-S dataset. Nevertheless, the reconstruction results show superior reliability compared with GLORYS2V4 over the entire 1993–2023 period. This demonstrates that the model’s learning capability is not restricted to the temporal range of the training data and possesses strong generalization ability.

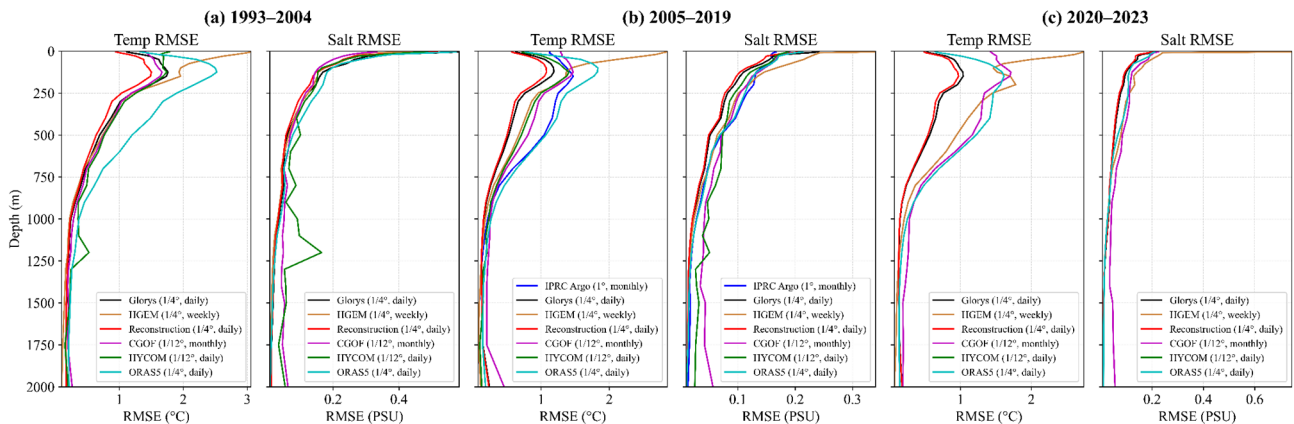


Figure 16: RMSE profiles of different temperature and salinity datasets compared with WOD T-S profiles during (a) 1993–2004, (b) 2005–2019, and (c) 2020–2023.

The variation of RMSE with depth showed in Fig. 16 indicates that, throughout the entire evaluation period, the reconstructed temperature consistently exhibits the lowest RMSE at all depth levels compared with other temperature datasets. For salinity, during 1993–2004, the CGOF salinity data show a slight advantage at depths shallower than 130 m; however, below 130 m, the reconstructed salinity data remain more consistent with the WOD salinity profiles (Fig. 16a). During 2005–2019, the IPRC Argo salinity dataset achieves the lowest RMSE near the surface (50 m), while at all other depths, the reconstructed salinity data better match the in situ observations (Fig. 16b). Overall, the reconstructed T-S fields exhibit high reliability and stability across all depth layers, further confirming the robustness and accuracy of the proposed reconstruction approach.

To more intuitively illustrate the relationships between various T-S datasets and the WOD T-S profiles, four representative depths (50 m, 200 m, 800 m, and 1000 m) were selected. At each depth, density scatter plots were drawn for the reconstructed T-S data, as well as for the GLORYS2V4, HGEM, IPRC Argo, and CGOF datasets, in comparison with the WOD in situ observations. The density scatter plots of temperature and salinity data are shown in Fig. 17 and Fig. 18, respectively.

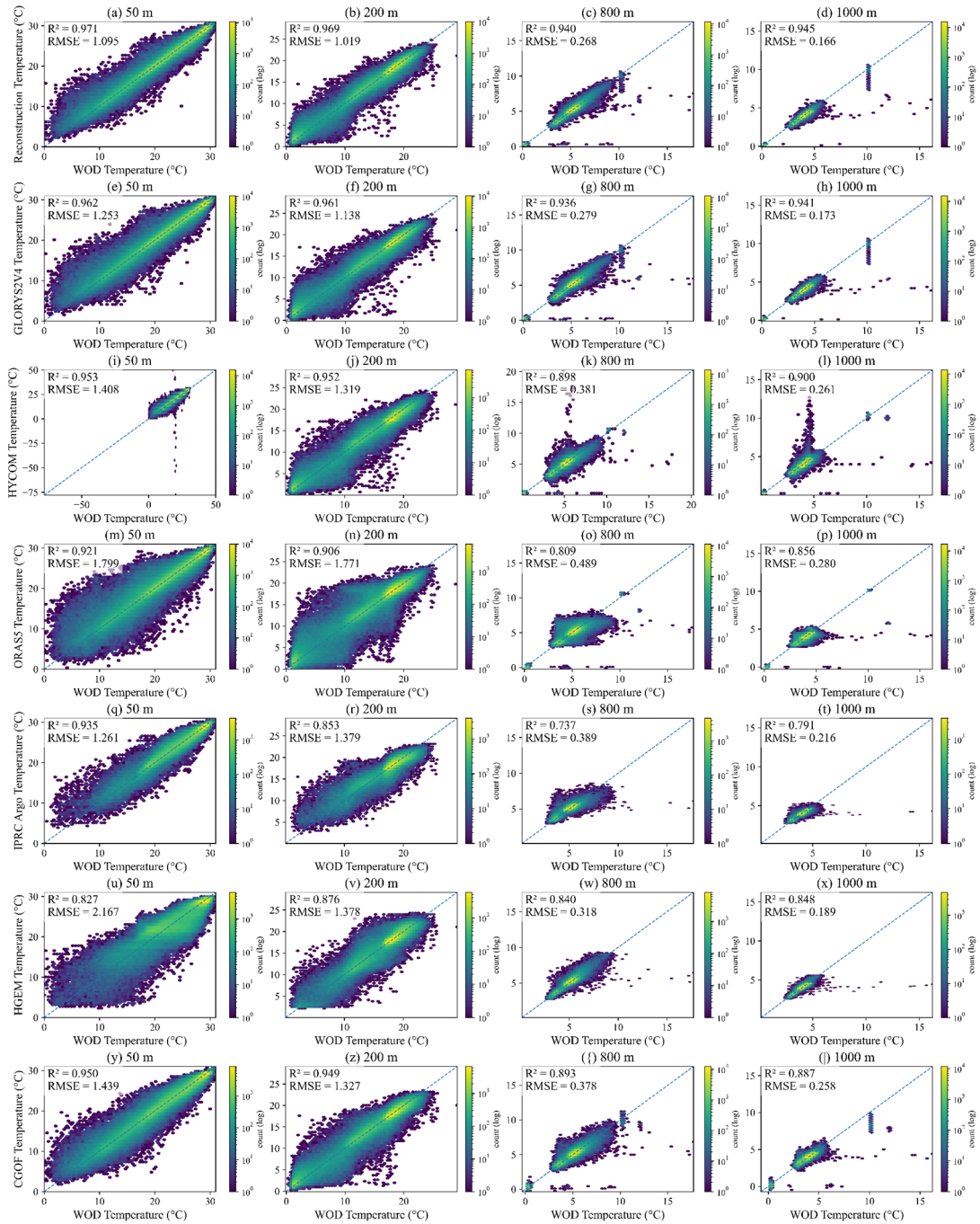


Figure 17. Density scatter plots between different temperature datasets and WOD observed temperature profiles at four representative depths (50 m, 200 m, 800 m, and 1000 m) over the period of 1993–2023.

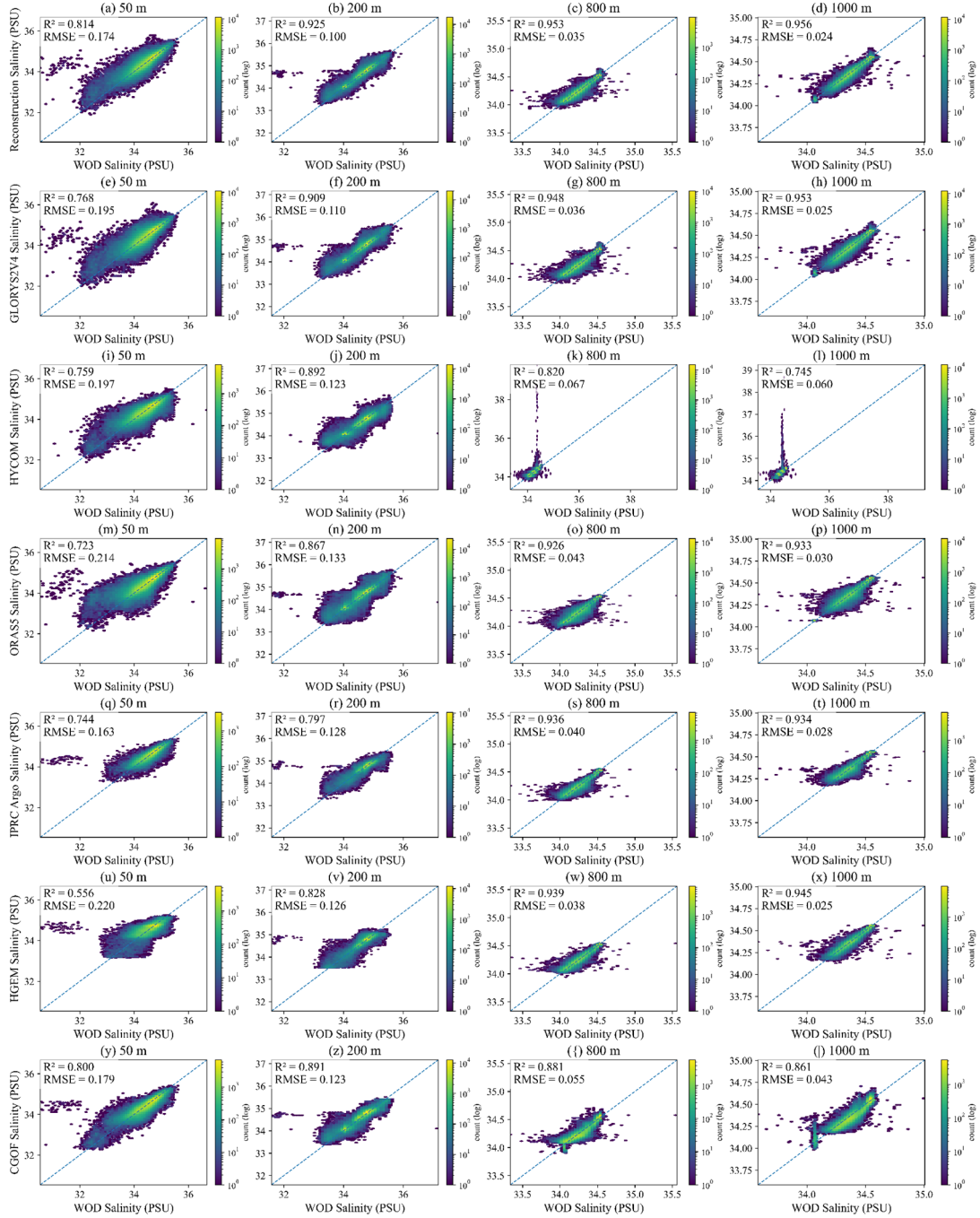


Figure 18. Density scatter plots between different salinity datasets and WOD observed salinity profiles at four representative depths (50 m, 200 m, 800 m, and 1000 m) over the period of 1993-2023.

From Figs.17-18, the correlations and systematic bias characteristics between each dataset and the WOD in situ observations at different depths can be clearly identified. The reconstructed results proposed in this study exhibit the highest consistency and the most compact distribution across all the four representative depths. The scatter clouds are densely concentrated along the 1:1 diagonal line, with distinct density peaks and narrow bias distributions. It indicates that the model can accurately reproduce the real oceanic thermohaline structure on a large scale.

At the surface layer (50 m), influenced by air–sea exchanges and seasonal mixing, all datasets show a certain degree of dispersion. However, the reconstructed results demonstrate the smallest dispersion range, with almost no systematic overestimation or underestimation. In contrast, GLORYS2V4 and CGOF exhibit slight offsets in regions of high temperature and salinity, reflecting weaker responses in strongly variable areas. At 200 m depth, the relationship between the reconstructed results and the WOD observations becomes more linear, suggesting that the model effectively captures the thermohaline gradient structure near the upper boundary of the pycnocline. The HGEM and Argo products show slightly more scattered distributions at this depth, indicating moderate biases in reproducing the upper-to-mid-layer thermohaline structure. In the intermediate and deep layers (800 m and 1000 m), the reconstructed results maintain excellent agreement with the observations, with highly concentrated scatter and very low RMSE values. This demonstrates that the model performs not only well at the surface but also robustly reconstructs deep thermohaline structures. In comparison, GLORYS2V4 and CGOF exhibit slightly broader scatter distributions, showing a systematic underestimation trend, while HGEM displays increased dispersion, reflecting weaker deep-layer constraints.

Overall, the density scatter distributions for both temperature and salinity confirm that the reconstructed data have the highest correlation and lowest errors relative to the WOD observations, maintaining consistent performance across all depths. These results verify the high accuracy and robustness of the proposed reconstruction method under multi-scale and multi-depth conditions. Furthermore, they indicate that the developed neural network model effectively integrates multi-source information during the long-term reconstruction process—capturing rapid upper-ocean variability while accurately restoring deep-layer equilibrium structures—thus providing a solid foundation for high-quality three-dimensional thermohaline reanalysis.

4 Data availability

The data used in this study are available for consultation as described in Section 2.1. The T-S data reconstructed using the method proposed in this study are freely accessible at <https://doi.org/10.57760/sciencedb.31950> (Wang et al., 2025).

5 Discussion and Conclusion

To achieve real-time and accurate reconstruction of daily three-dimensional T-S fields ($1/4^\circ$, 26 layers, 5–2000 m) in the northwestern Pacific ($0\text{--}40^\circ\text{N}$, $120\text{--}160^\circ\text{E}$), this study proposes an attention-enhanced 3D U-Net++ reconstruction framework that relies solely on real-time available SST and SSH data. The attention enhanced 3D U-Net++ architecture provides a mechanism for cross-scale feature aggregation and selective information gating through deep skip connections. The attention gates highlight temporal surface features that are more strongly correlated with the target depth layers along the multi-resolution pathways, thereby mitigating noise propagation and over-smoothing. Combined with the 3D encoder–decoder structure, this design enhances the preservation of vertical gradients and frontal structures in the reconstructed fields. The network takes 26 consecutive days of SST and SSH as input, which effectively alleviates the intrinsic challenge of mapping from limited surface inputs to full-depth outputs. A single-time surface-to-volume mapping is inherently underdetermined, resembling a super-resolution problem. By incorporating inter-day evolution, the model can extract implicit constraints associated with subseasonal variability, circulation, and mixing processes from the temporal continuity of surface signals, thereby reducing non-uniqueness and improving the discriminability of vertical structures. In addition, a transfer learning strategy is employed. The model is first pretrained using monthly SST/SSH and IPRC-Argo datasets to learn observation-dominated low-frequency spatiotemporal signals and stable structures. It is then retrained using daily SST/SSH and GLORYS2V4 data to capture the dynamic processes and assimilation mechanisms embedded in the reanalysis fields.

Analysis results demonstrate that, both on the validation set and in long-term statistical evaluations, the reconstructed T-S fields are more consistent with in situ observation profiles, verifying the reliability and accuracy of the proposed method for subsurface ocean data inversion. Despite the promising results, several limitations and uncertainties must be acknowledged. First, the computational cost of training is substantial due to the employment of operations such as 3D convolutions. Second, despite validation against in situ observations, the spatial sparsity of these profiles implies inherent uncertainty regarding the model’s reliability in unsampled regions.

The data obtained in this study provide crucial support for revealing mesoscale ocean dynamic processes. Furthermore, they lay a solid foundation for quantitatively estimating key elements, including ocean mass transport, heat, and salinity fluxes. In the future, these data will be valuable for advancing the study of mesoscale ocean dynamics. They also show great potential for improving ocean model simulations and enhancing climate prediction accuracy.

525 **Author contributions.**

HW and LZ conceptualized the study and contributed to the writing and revision of the manuscript. HW performed data processing, coding, and underwater temperature–salinity reconstruction. LZ, SY, and XY contributed to the discussion of results and critically reviewed the manuscript. ZL was responsible for data collection and partial code development.

Competing interests.

530 The contact author has declared that none of the authors has any competing interests.

Acknowledgement.

The authors gratefully acknowledge the use of the Optimum Interpolation Sea Surface Temperature (OISST) data provided by NOAA (<https://www.ncei.noaa.gov/data/sea-surface-temperature-optimum-interpolation/v2.1/access/avhrr/>), and the sea level data from the Archiving, Validation, and Interpretation of Satellite Oceanographic data (AVISO), available via
535 Copernicus Europe’s eyes on Earth (https://data.marine.copernicus.eu/product/SEALEVEL_GLO_PHY_L4_MY_008_047/description). We also
acknowledge the GLORYS2V4 reanalysis data for temperature and salinity gridded fields
(https://data.marine.copernicus.eu/product/GLOBAL_MULTIYEAR_PHY_ENS_001_031/description) and the Argo
monthly temperature and salinity gridded datasets provided by the International Pacific Research Center (IPRC,
540 http://apdrc.soest.hawaii.edu/projects/Argo/data/gridded/On_standard_levels/index-1.html).

Additional thanks are extended to the World Ocean Database for temperature–salinity profiles
(<https://www.ncei.noaa.gov/products/world-ocean-database>), the Oceanographic Data Center, Chinese Academy of
Sciences (CODC, <https://www.casodc.com/>), for the High-Resolution Northwest Pacific Temperature Salinity Current
Dataset, and the National Oceanic Cloud (<https://www.cmoc-china.cn>) for providing the China Global Ocean Fusion
545 Dataset 1.0.

This work was supported by the Oceanographic Data Center, Institute of Oceanology, Chinese Academy of Sciences (IOCAS).

Financial support.

This study was supported by the National Natural Science Foundation of China (42576027), the Project of Science and
550 Technology Innovation of Laoshan Laboratory (LSKJ202201702), and the TS Scholar Program (tsqn202103128).

References

- Ali, M. M., Swain, D., and Weller, R. A.: Estimation of ocean subsurface thermal structure from surface parameters: A neural network approach, *Geophys Res Lett*, 31, <https://doi.org/10.1029/2004gl021192>, 2004.
- 555 Bellucci, A., Masina, S., DiPietro, P., and Navarra, A.: Using Temperature–Salinity Relations in a Global Ocean Implementation of a Multivariate Data Assimilation Scheme, *Monthly Weather Review*, 135, 3785–3807, <https://doi.org/10.1175/2007MWR1821.1>, 2007.
- Chen, Y., Bao, S., Cao, Y., Zhang, W., and Wang, H.: The Yin-He Global Ocean Data Assimilation and Forecast System, *Ocean-Land-Atmosphere Research*, 4, 0121, <https://doi.org/10.34133/olar.0121>, 2025.
- 560 Chen, Z., Wang, P., Bao, S., and Zhang, W.: Rapid reconstruction of temperature and salinity fields based on machine learning and the assimilation application, *Frontiers in Marine Science*, Volume 9 - 2022, <https://doi.org/10.3389/fmars.2022.985048>, 2022.
- Cheng, H., Sun, L., and Li, J.: Neural Network Approach to Retrieving Ocean Subsurface Temperatures from Surface Parameters Observed by Satellites, *Water*, 13, 388, <https://doi.org/10.3390/w13030388>, 2021.
- 565 Cheng, L., Zhu, J., Cowley, R., Boyer, T., and Wijffels, S.: Time, probe type, and temperature variable bias corrections to historical expendable bathythermograph observations, *J Atmos Ocean Tech*, 31, 1793–1825, <https://doi.org/10.1175/JTECH-D-13-00197.1>, 2014.
- Curry, R., Dickson, B., and Yashayaev, I.: A change in the freshwater balance of the Atlantic Ocean over the past four decades, *Nature*, 426, 826–829, <https://doi.org/10.1038/nature02206>, 2003.
- 570 Fu, L. and Davidson, R.: A note on the barotropic response of sea level to time-dependent wind forcing, *Oceanographic Literature Review*, 8, 757, <https://doi.org/10.1029/95JC02259>, 1996.
- Fu, W.: On the Role of Temperature and Salinity Data Assimilation to Constrain a Coupled Physical–Biogeochemical Model in the Baltic Sea, *J Phys Oceanogr*, 46, 713–729, <https://doi.org/10.1175/JPO-D-15-0027.1>, 2016.
- Gill, A. E.: *Atmosphere—ocean dynamics*, Elsevier, 2016.
- 575 Gilson, J., Roemmich, D., Cornuelle, B., and Fu, L. L.: Relationship of TOPEX/Poseidon altimetric height to steric height and circulation in the North Pacific, *J Geophys Res-Oceans*, 103, 27947–27965, <https://doi.org/10.1029/98jc01680>, 1998.
- Guinehut, S., Dhomps, A. L., Larnicol, G., and Le Traon, P. Y.: High resolution 3-D temperature and salinity fields derived from in situ and satellite observations, *Ocean Sci*, 8, 845–857, <https://doi.org/10.5194/os-8-845-2012>, 2012.
- Gwyther, D. E., Keating, S. R., Kerry, C., and Roughan, M.: How does 4DVar data assimilation affect the vertical representation of mesoscale eddies? A case study with observing system simulation experiments (OSSEs) using ROMS v3.9, *Geosci. Model Dev.*, 16, 157–178, <https://doi.org/10.5194/gmd-16-157-2023>, 2023.
- 580 Huang, B. Y., Liu, C. Y., Banzon, V., Freeman, E., Graham, G., Hankins, B., Smith, T., and Zhang, H. M.: Improvements of the Daily Optimum Interpolation Sea Surface Temperature (DOISST) Version 2.1, *J Climate*, 34, 2923–2939, <https://doi.org/10.1175/Jcli-D-20-0166.1>, 2021.
- Huang, R. X.: *Ocean circulation: wind-driven and thermohaline processes*, Cambridge University Press, 2010.
- 585 Isern-Fontanet, J., Chapron, B., Lapeyre, G., and Klein, P.: Potential use of microwave sea surface temperatures for the estimation of ocean currents, *Geophys Res Lett*, 33, <https://doi.org/10.1029/2006gl027801>, 2006.
- Klemas, V. and Yan, X. H.: Subsurface and deeper ocean remote sensing from satellites: An overview and new results, *Prog Oceanogr*, 122, 1–9, <https://doi.org/10.1016/j.pocean.2013.11.010>, 2014.
- 590 LaCasce, J. H. and Mahadevan, A.: Estimating subsurface horizontal and vertical velocities from sea-surface temperature, *Journal of Marine Research*, 64(5), 695–721, https://doi.org/https://elischolar.library.yale.edu/journal_of_marine_research/144, 2006.
- Mao, K., Liu, C., Zhang, S., and Gao, F.: Reconstructing Ocean Subsurface Temperature and Salinity from Sea Surface Information Based on Dual Path Convolutional Neural Networks, *Journal of Marine Science and Engineering*, 11, 1030, <https://doi.org/10.3390/jmse11051030>, 2023.
- 595 Martin, M. J., Hoteit, I., Bertino, L., and Moore, A. M.: Data assimilation schemes for ocean forecasting: state of the art, *Ocean prediction: present status and state of the art (OPSR)*, 5, 9, <https://doi.org/10.5194/sp-5-oprsr-9-2025>, 2025.

- Mishonov, A. V., Boyer, T. P., Baranova, O. K., Bouchard, C. N., Cross, S. L., Garcia, H. E., Locarnini, R. A., Paver, C. R., Reagan, J. R., Wang, Z., Seidov, D., Grodsky, A. I., and Beauchamp, J. G.: World Ocean Database 2023, <https://doi.org/10.25923/z885-h264>, 2024.
- 600 Munk, W. H.: On the Wind-Driven Ocean Circulation, *J Meteorol*, 7, 79–93, [https://doi.org/10.1175/1520-0469\(1950\)007<0080:OTWDOC>2.0.CO;2](https://doi.org/10.1175/1520-0469(1950)007<0080:OTWDOC>2.0.CO;2), 1950.
- Pan, S. J. and Yang, Q.: A Survey on Transfer Learning, *Ieee T Knowl Data En*, 22, 1345–1359, <https://doi.org/10.1109/TKDE.2009.191>, 2010.
- 605 Pauthenet, E., Bachelot, L., Balem, K., Maze, G., Tréguier, A. M., Roquet, F., Fablet, R., and Tandeo, P.: Four-dimensional temperature, salinity and mixed-layer depth in the Gulf Stream, reconstructed from remote-sensing and in situ observations with neural networks, *Ocean Sci.*, 18, 1221–1244, <https://doi.org/10.5194/os-18-1221-2022>, 2022.
- Pilo, G. S., Oke, P. R., Coleman, R., Rykova, T., and Ridgway, K.: Impact of data assimilation on vertical velocities in an eddy resolving ocean model, *Ocean Modelling*, 131, 71–85, <https://doi.org/10.1016/j.ocemod.2018.09.003>, 2018.
- 610 Smith, P. A. H., Sørensen, K. A., Buongiorno Nardelli, B., Chauhan, A., Christensen, A., St. John, M., Rodrigues, F., and Mariani, P.: Reconstruction of subsurface ocean state variables using Convolutional Neural Networks with combined satellite and in situ data, *Frontiers in Marine Science*, Volume 10 - 2023, <https://doi.org/10.3389/fmars.2023.1218514>, 2023.
- Song, T., Xu, G., Yang, K., Li, X., and Peng, S.: Convformer: A Model for Reconstructing Ocean Subsurface Temperature and Salinity Fields Based on Multi-Source Remote Sensing Observations, *Remote Sensing*, 16, 2422, <https://doi.org/10.3390/rs16132422>, 2024.
- 615 Stewart, R. H.: Introduction to physical oceanography, 2008.
- Su, H., Yang, X., Lu, W., and Yan, X.-H.: Estimating Subsurface Thermohaline Structure of the Global Ocean Using Surface Remote Sensing Observations, *Remote Sensing*, 11, 1598, <https://doi.org/10.3390/rs11131598>, 2019.
- 620 Su, H., Jiang, J., Wang, A., Zhuang, W., and Yan, X.-H.: Subsurface Temperature Reconstruction for the Global Ocean from 1993 to 2020 Using Satellite Observations and Deep Learning, *Remote Sensing*, 14, 3198, <https://doi.org/10.3390/rs14133198>, 2022.
- Su, H., Wang, A., Zhang, T., Qin, T., Du, X., and Yan, X.-H.: Super-resolution of subsurface temperature field from remote sensing observations based on machine learning, *Int J Appl Earth Obs*, 102, 102440, <https://doi.org/10.1016/j.jag.2021.102440>, 2021.
- 625 Talley, L. D., Pickard, G. L., Emery, W. J., and Swift, J. H.: Chapter 6 - Data Analysis Concepts and Observational Methods, in: *Descriptive Physical Oceanography (Sixth Edition)*, Academic Press, Boston, 147–186, <https://doi.org/10.1016/B978-0-7506-4552-2.10006-X>, 2011.
- Tran, D., Bourdev, L., Fergus, R., Torresani, L., and Paluri, M.: Learning Spatiotemporal Features with 3D Convolutional Networks, 2015 IEEE International Conference on Computer Vision (ICCV), 7–13 Dec. 2015, 4489–4497, <https://doi.org/10.1109/ICCV.2015.510>,
- 630 Wang, H., Song, T., Zhu, S., Yang, S., and Feng, L.: Subsurface Temperature Estimation from Sea Surface Data Using Neural Network Models in the Western Pacific Ocean, *Mathematics*, 9, 852, <https://doi.org/10.3390/math9080852>, 2021.
- Wang, H., Zhang, L., Yang, S., Yan, X., and Li, Z.: Attention Enhanced 3D-U-Net++ Ocean Temperature and Salinity Reconstruction in the Northwestern Pacific based on Transfer Learning [data set], <https://doi.org/10.57760/sciencedb.31950>, 2025.
- 635 Willis, J. K., Roemmich, D., and Cornuelle, B.: Combining altimetric height with broadscale profile data to estimate steric height, heat storage, subsurface temperature, and sea-surface temperature variability, *J Geophys Res-Oceans*, 108, 3292, <https://doi.org/10.1029/2002jc001755>, 2003.
- Woo, S. H., Park, J., Lee, J. Y., and Kweon, I. S.: CBAM: Convolutional Block Attention Module, *Lect Notes Comput Sc*, 11211, 3–19, https://doi.org/10.1007/978-3-030-01234-2_1, 2018.
- 640 Wu, X. B., Yan, X. H., Jo, Y. H., and Liu, W. T.: Estimation of Subsurface Temperature Anomaly in the North Atlantic Using a Self-Organizing Map Neural Network, *J Atmos Ocean Tech*, 29, 1675–1688, <https://doi.org/10.1175/Jtech-D-12-00013.1>, 2012.

- 645 Xie, H. R., Dong, C. M., and Xu, Q.: Dual U-Vision-Transformer for reconstructing the three-dimensional eddy-resolving oceanic physical parameters from satellite observations, *Int J Appl Earth Obs*, 136, <https://doi.org/10.1016/j.jag.2025.104382>, 2025.
- Yu, X., Yi, D. L., and Wang, P.: Enhancing Ocean Temperature and Salinity Reconstruction with Deep Learning: The Role of Surface Waves, *Journal of Marine Science and Engineering*, 13, 910, <https://doi.org/10.3390/jmse13050910>, 2025.
- 650 Zhang, L. and Sun, C.: A geostrophic empirical mode based on altimetric sea surface height, *Sci China Earth Sci*, 55, 1193–1205, <https://doi.org/10.1007/s11430-011-4293-z>, 2012.
- Zhang, Y. Y., Liu, Y. H., Kong, Y., and Hu, P.: An Improved Method for Retrieving Subsurface Temperature Using the ConvLSTM Model in the Western Pacific Ocean, *Journal of Marine Science and Engineering*, 12, <https://doi.org/10.3390/jmse12040620>, 2024.
- 655 Zhao, Q., Li, S., Cai, Y., Zhong, G., and Peng, S.: Reconstruction of the Subsurface Temperature and Salinity in the South China Sea Using Deep-Learning Techniques with a Physical Guidance, *Remote Sensing*, 17, 2954, <https://doi.org/10.3390/rs17172954>, 2025.
- Zhou, Z. W., Siddiquee, M. M. R., Tajbakhsh, N., and Liang, J. M.: UNet plus plus : A Nested U-Net Architecture for Medical Image Segmentation, *Deep Learning in Medical Image Analysis and Multimodal Learning for Clinical Decision Support, Dlmia 2018*, 11045, 3–11, https://doi.org/10.1007/978-3-030-00889-5_1, 2018.
- 660